



Enhancing the visible light absorbance of $\text{Bi}_2\text{Ti}_2\text{O}_7$ through Fe-substitution and its effects on photocatalytic hydrogen evolution

Bradley Allured^a, Steven Delacruz^b, Timothy Darling^a, Muhammad N. Huda^c,
Vaidyanathan (Ravi) Subramanian^{b,*}

^a Department of Physics, University of Nevada, Reno, United States

^b Chemical and Materials Engineering, University of Nevada, Reno, United States

^c Physics Department, University of Texas, Arlington, United States

ARTICLE INFO

Article history:

Received 13 March 2013

Received in revised form 6 June 2013

Accepted 3 July 2013

Available online 13 July 2013

Keywords:

Pyrochlore

Bismuth titanate

Fe- $\text{Bi}_2\text{Ti}_2\text{O}_7$

Hydrogen

Photocatalysis

ABSTRACT

The visible light-driven, photo-assisted hydrogen generation using a pyrochlore-type photocatalyst ($\text{A}_2\text{B}_2\text{O}_7$), containing an earth-abundant element for boosting photoactivity, is presented. A wet chemical approach has been used for the synthesis of the pyrochlore photocatalyst. The characterization of the material using surface and optical techniques indicates that Fe can be successfully incorporated into $\text{Bi}_2\text{Ti}_2\text{O}_7$ (BTO) with varying concentrations. The photocatalytic activity of the material was examined by performing hydrogen generation from a methanol–water mixture under UV–vis illumination in a slurry reactor. The wavelength range of visible light absorbed is improved by 100–200 nm depending on Fe doping, and a corresponding increase in photocatalytic activity is noted. Replacing 1 mol% of the Bi with Fe in the BTO (referred to below as 1% Fe doped or 1% Fe-BTO) is noted to be optimal in improving photocatalytic hydrogen generation, with more heavily doped samples showing progressively lower improvement.

© 2013 Elsevier B.V. All rights reserved.

1. Introduction

Hydrogen as an energy source is of considerable interest on account of the different pathways to its usage (e.g. fuel cell or combustion), its reputation as a clean energy carrier, and being a carbon-free source of energy generation that can be produced from a variety of hydrocarbons [1–3]. One approach is to produce hydrogen using a photocatalytic process, mostly using oxides as photoactivators [4–6]. This process is attractive since it employs sunlight and water – two abundant, ecologically beneficial, and readily available natural resources. Oxides are desirable photocatalysts to facilitate water splitting since they are stable under most operating conditions [7]. Among oxides, the most popular strategy has been to use TiO_2 and its composites [8–10]. TiO_2 alone has been shown to be ineffective, but it exhibits potential as a composite when: (i) doped [11], (ii) coupled with a visible light absorber (VLA) [12], or (iii) coupled with a VLA plus other additives [13] to improve charge separation/photocatalytic efficiencies. Several reviews have discussed the merits of these and

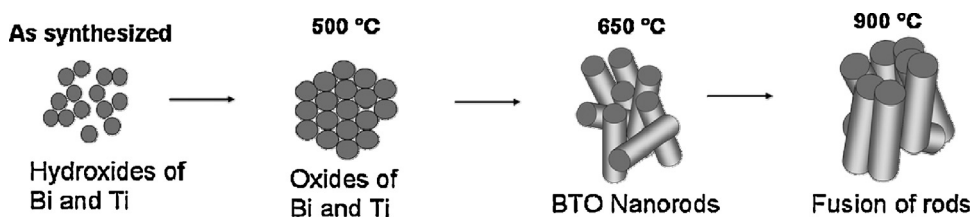
other approaches at length [14–19]. However, the formation of composites almost always requires intricate synthesis protocols, increases the potential for instability with every additional layer, and raises the possibility of inefficient charge separation due to multistep electron transport process.

TiO_2 as a host for inclusion of metal ions has been extensively explored previously [20]. Unlike single metal oxide structures such as TiO_2 , structures that can incorporate multiple elements in the basic unit cell offer an additional degree of freedom to design photocatalysts. In principle, one can tune the optical, electronic, and photocatalytic properties within the host unit cell much more effectively, provided that the host cell can be thermodynamically stable with multiple cations. This is in contrast to the scenario for simple doping in metal-oxides, where structural deterioration due to doping is common. Achieving good crystallinity with the addition of external impurities in a metal-oxide is a huge challenge. The pyrochlore $\text{A}_2\text{B}_2\text{O}_7$ is one such multi-cation complex made of a simpler fluorite type of structure (AO_2 and its multiples) [21]. This structure can be photoactive [22,23]. The cationic sites A and B can be independently populated with different elements, allowing for a high degree of compositional variance such as $\text{A}_2\text{B}_{2-x}\text{B}'_x\text{O}_7$ and $\text{A}_{2-x}\text{A}'_x\text{B}_2\text{O}_7$ where A'/B' is a third cation [24,25].

Recently, our group demonstrated the synthesis of a multi-metal oxide using the earth-abundant elements Bi, Ti, and O in the pyrochlore structure by applying a cost-effective reverse

* Corresponding author at: Department of Chemical and Materials Engineering, University of Nevada, Reno – 89557, United States. Tel.: +1 775 784 4686; fax: +1 775 327 5059.

E-mail address: ravisv@unr.edu (V. Subramanian).



Scheme 1. Heat treatment can be used as a stand-alone approach to control the size and shape of oxide pyrochlores when the precursors are synthesized using a wet chemical reverse micelle-based approach.

micelle-based technique [26]. The key discovery was an approach to tuning the chemical and physical features of the same amorphous BTO, as shown in Scheme 1. Using the same amorphous samples, aspect ratios can be controlled by simply varying the temperature. The work discussed here concerns a universal approach to efficient synthesis of both BTO pyrochlore nanoparticles, as well as composites with additives in it. With a bandgap of 2.82 eV, the $\text{Bi}_2\text{Ti}_2\text{O}_7$ photocatalyst demonstrates visible light absorbance (comparable to similar photocatalysts of its class) and UV-vis driven photocatalytic activity.

Though the BTO is visible light active [27–30], its absorbance and photoactivity have significant potential for further improvement. The goal is the development of a material that can absorb further into the visible region, without sacrificing the quality of its photoactivity. The incorporation of an additional earth-abundant element to improve BTO's optical properties and photoactivity is essential, and this work presents a strategy in that direction. Specifically, an approach to synthesize BTO that incorporates Fe, while retaining the pyrochlore structure, is discussed. The optical, surface, structural, and photocatalytic properties of the Fe-BTO and the effects of Fe concentration in the Fe-BTO have been systematically examined. It is shown that the inclusion of Fe in BTO improves visible light absorbance and, in certain concentrations, boosts the ensuing photocatalytic activity of BTO, as demonstrated through photocatalytic hydrogen generation.

2. Experimental

2.1. Chemicals

Nitric acid (ACS, BDH3046-2.5LPC, 68%, BDH Aristar), bismuth nitrate pentahydrate (ACS, 98%, Alfa Aesar), titanium(IV) isopropoxide (97%, Sigma–Aldrich), iron(III) nitrate nonahydrate (ACS, $\geq 98\%$, Sigma–Aldrich), and ammonia solution (A667-212, $\geq 25\%$, Fisher Scientific) were obtained from commercial vendors as indicated in brackets. Ultra high purity, deionized water for synthesis was obtained using a Millipore® system. The chemicals were used “as is” without any alterations for the preparation of the following precursor solutions: Titanium isopropoxide was reacted with a small amount of water, dissolved in 16.3 M nitric acid, and then diluted to the equivalent of a 0.1 M solution in 1 M nitric acid. This solution was used immediately in further synthesis. The nitric acid was diluted in water to 1 M. 0.1 M bismuth nitrate and 0.1 M iron nitrate solutions were prepared in the nitric acid with vigorous stirring.

2.2. Synthesis approach

The procedure presented here is different from, but based on, the reverse micelle approach reported earlier for BTO synthesis [26]. 50 mL of the titanium isopropoxide precursor and bismuth nitrate precursor were added to a 250 mL beaker. Iron nitrate solution was added as the third cation (in place of an equal volume of the Bi solution) in the ternary system. A magnetic stirrer was

used to ensure that the beaker contents were well stirred, while 50 mL of strong ammonia was gradually added to the beaker to increase the pH. The resulting suspension was allowed to settle and the supernatant liquid was removed. The precipitate was then transferred into a centrifuge tube and separated over two minutes.

The precipitate was washed with deionized water and centrifuged again. This step was repeated three times. The solid residue was then scraped and dried in an oven between 150 °C and 190 °C for several hours, depending upon the volume of material prepared. A mortar and pestle was used to crush the dried material into a fine powder. The samples were then calcinated in a furnace at 600 °C for 4 h in a configuration where a covered crucible contains bismuth chloride or bismuth oxide, and a smaller, open crucible is nested inside, seated in the bismuth chloride. The presence of bismuth chloride is meant to increase the Bi vapor pressure and reduce the chemical potential for the extrusion of metallic bismuth. Without the nested configuration, we found the low melting point of bismuth caused the formation of unwanted oxides in our samples, but the presence of BiCl effectively suppresses the extrusion of metallic Bi as evidenced by the BTO signature, and lack of unwanted oxide signatures, in X-ray diffraction (XRD). The furnace temperature rose from room temperature to 600 °C in the first 2 h, stayed constant at 600 °C for 4 h, and decreased from 600 °C back to room temperature in the last hour. Fig. 1 provides an outline of the steps for the synthesis of Fe-BTO.

2.3. Material characterization

The characterization of the oxide photocatalysts was performed using several complementary tools. An Hitachi® S-4700 scanning electron microscope (SEM) was used to examine the physical features of the powder. An attached electron dispersive spectrometer (EDS) was used to determine the photocatalyst composition. Crystalline features of the photocatalysts were examined using an XRD instrument from Philips (model: 12045 B/3 X-ray diffractometer) with a scan rate of 0.03°/min. High resolution transmission electron microscopy ((HR)TEM) analysis was performed using a JEOL® 2100F instrument equipped with a selected area electron diffraction (SAED) analyzer. The optical properties of the powder were examined using a UV–vis diffuse reflectance measurement with a Shimadzu UV-2501PC spectrophotometer.

2.4. Determination of photocatalytic properties

The photocatalytic reactions were performed in a slurry reactor, the details of which are given in previous work [26]. Briefly, a tubular vessel of 500 mL volume, with an option to introduce a lamp in the annulus with jacketed temperature control achieved using a stream of cooling water, was used as the reaction setup. The lamp was a 450 W Hg vapor source. 0.150 g of the photocatalyst was used in every experimental run and suspended by continuous stirring to ensure homogenous distribution. The suspension was de-aerated

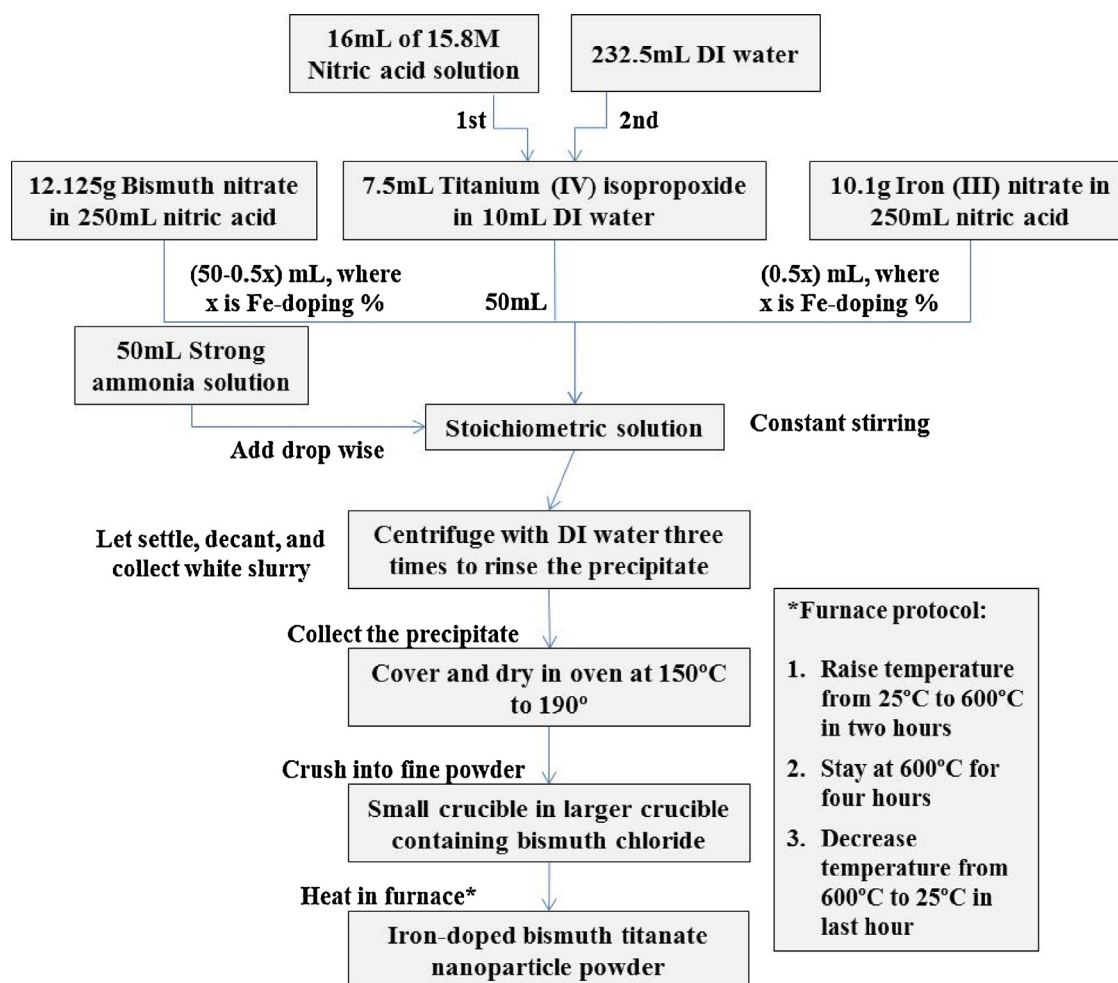


Fig. 1. The scheme shows the step-by-step details that include the wet processing and thermal treatment stages followed for the synthesis of bismuth titanate (BTO) and BTO with varying Fe content (Fe-BTO).

first (to remove dissolved oxygen) using Ar gas for 20 min and then illuminated. The evolved gases were collected using downward displacement of water in a column. A gas chromatograph (GC) equipped with a thermal conductivity detector (TCD) (SRI 8610C) was used for hydrogen detection. All experiments were performed multiple times to ensure consistency and reproducibility.

3. Results

3.1. Characterization of the photocatalyst

3.1.1. SEM analysis

The synthesized products were first examined for information regarding their physical features using an SEM. Fig. 2A shows a representative image of the samples without Fe. Fig. 2B–D shows SEM images with varying Fe content. The particle morphology and shape are almost identical in the absence and presence of Fe. The addition of varying percentages of Fe also does not show a significant change in the physical appearances. In general, the particles demonstrate dimensions of 50 ± 15 nm. However, the uncalcinated samples showed a broader size distribution and were more dissimilar. In a close and relevant article, particles prepared by combining Bi, Fe, and Ti to form an oxide using a wet chemical approach were reported as having relatively larger grain sizes upwards of 80 nm. The compound belongs to the pyrochlore family with a structure/composition of $(\text{Fe}_{0.2}\text{Bi}_{0.8})_2\text{Ti}_2\text{O}_7$ [31].

3.1.2. (HR)TEM analysis

Further examination of the particle morphology was performed using the (HR)TEM. The TEM image of an Fe-introduced composite complements the SEM analysis, in that the particle shape at different loading resembles the SEM results. Fig. 3 shows the (HR)TEM image of a representative Fe-introduced composite, 1% Fe-BTO. The presence of distinct patterns is evident across the samples. The SAED image shown in the insert of Fig. 3 confirms that the photocatalyst is polycrystalline. This observation indicates that the samples after heat treatment have undergone a phase transformation. The presence of an interplanar spacing of 3.2 nm corresponds to the (6 2 2) plane of the bismuth titanate [32].

3.1.3. EDS analysis

An EDS analyzer attached to the SEM was used as a screening tool to qualitatively confirm the presence of the various elements in the synthesized photocatalyst. Of particular interest was to confirm that the Fe addition during the synthesis stage actually becomes an integral part of the photocatalyst and is not washed away. EDS analysis confirms that all intended elements – Fe, Ti, Bi, and O – participate in the formation of the photocatalyst. Though the EDS analysis is regarded as qualitative and an evidence of the purity of the composite, the relative concentrations are reasonably close to the expected values, except for oxygen, which indicates there may be an oxygen deficiency. Along with the screening using EDS, XRD of these samples was carried out (as discussed in the next section) to determine the identity and structure of the photocatalyst. Thus, the

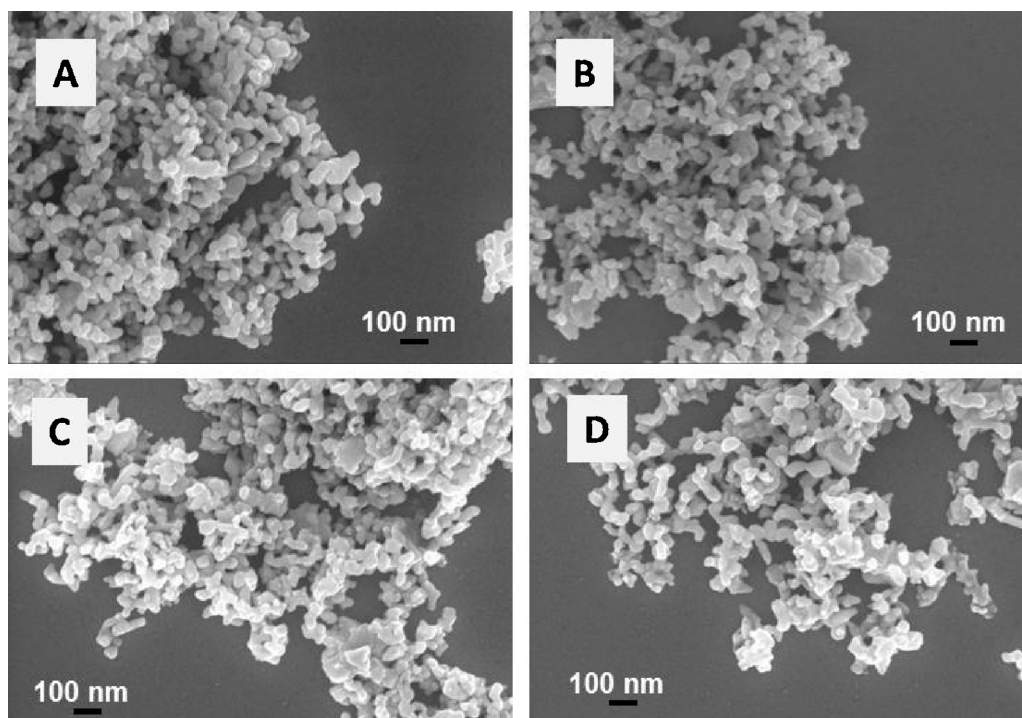


Fig. 2. The scanning electron microscope images of (A) BTO, (B) 1% Fe-BTO, (C) 2% Fe-BTO, and (D) 3% Fe-BTO after thermal treatment reveals the physical details (shape and size) of the photocatalysts.

SEM, (HR)TEM, and EDS analysis indicate that the synthesis method allows for (i) introduction of Fe and (ii) no significant alterations to the physical features (shape) of the photocatalysts, an essential prerequisite for critical comparison of photocatalytic performance.

3.1.4. XRD analysis

Since (HR)TEM alone cannot be used to identify the phase of the photocatalyst, XRD was performed to examine the photocatalyst

identity and validate the HRTEM findings. Fig. 4A shows the XRD results of the Fe-free composite after heat treatment. The presence of several peaks indicates that the photocatalyst is polycrystalline. The key peaks of interest are the 100% peaks corresponding to $2\theta = 29.99^\circ$, which indicate that the photocatalyst is BTO and belongs to the pyrochlore phase. The peaks are indexed to the JCPDS card # 32-0118. The uncalcined samples did not show any peaks, indicating that the materials have to be heat treated to undergo the phase transformation [31].

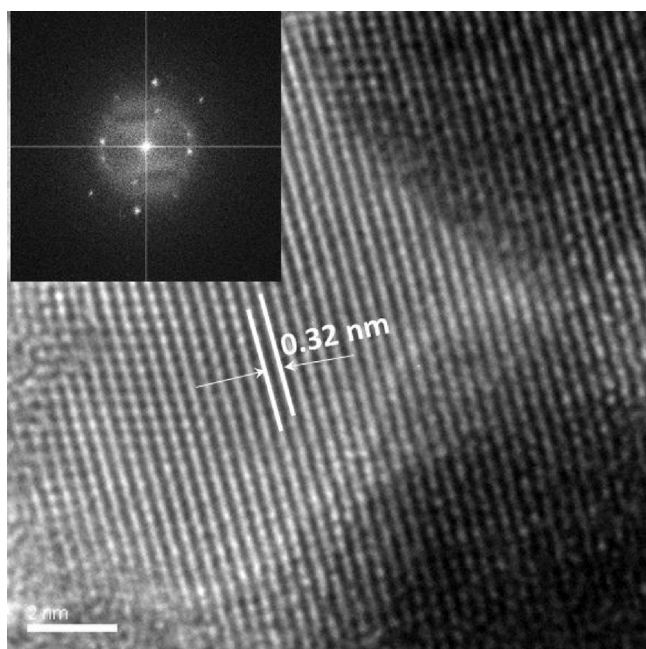


Fig. 3. The high resolution transmission electron microscopy ((HR)TEM) image of 1% Fe-BTO and (inset) the selected area electron diffraction (SAED) pattern of the sample, both confirm the crystalline nature of the photocatalyst.

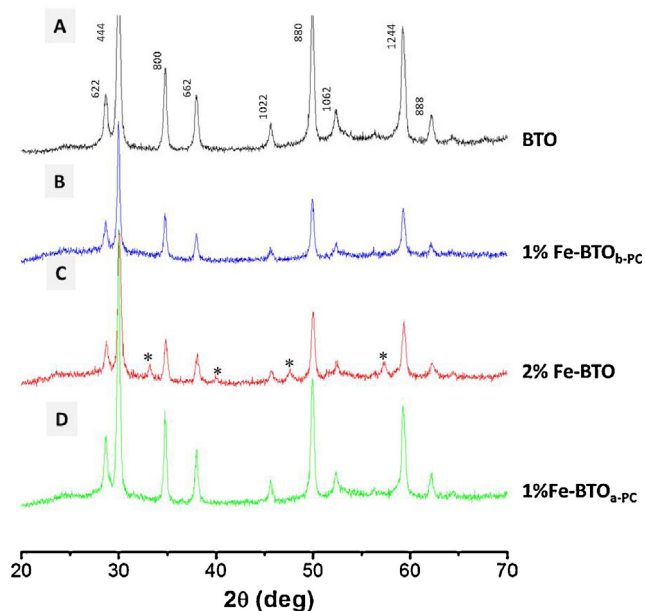


Fig. 4. The X-ray diffraction patterns of the (A) BTO, (B) 1% Fe-BTO (before photocatalysis), (C) 2% Fe-BTO, and (D) 1% Fe-BTO (after photocatalysis). The * in (C) indicate the Fe_2O_3 phase. The subscripts b-PC and a-PC represents before and after photocatalysis respectively.

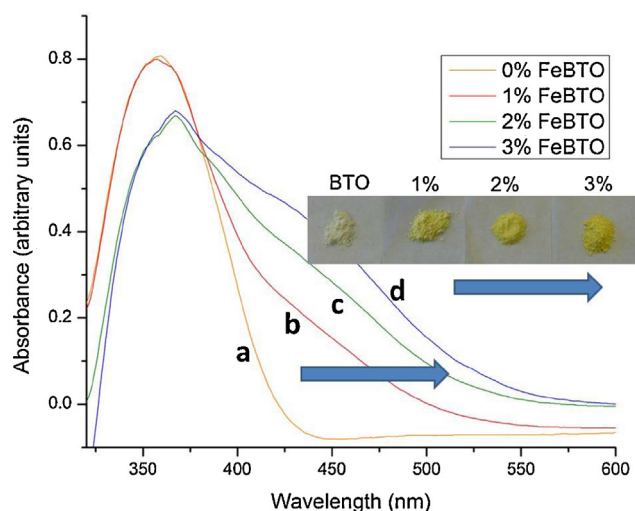


Fig. 5. The optical absorbance spectra of (a) BTO, (b) 1% Fe-BTO, (c) 2% Fe-BTO, and (d) 3% Fe-BTO are shown. The photographs of the respective samples indicating a gradual red shift in the coloration with increasing Fe content complements the absorbance spectra. (For interpretation of the references to color in this figure legend, the reader is referred to the web version of this article.)

The XRD of the 1% Fe-BTO, Fig. 4B, shows additional interesting observations. Firstly, a close examination in the 2θ region of $25\text{--}35^\circ$ and $40\text{--}50^\circ$ indicated no additional peaks. This is promising since the presence of additional peaks in this area would indicate that new phases are being formed, which is undesirable. If any Fe-based oxides were to be formed, they would have manifested as a peak or a broad peak with a shoulder in the region. Inclusion of an element within a structure is often indicated with the broadening of the 100% peak of the primary structure – BTO in this case. Similar observations were also noted with other Fe loadings, but evidence of small amounts of Fe_2O_3 can be seen in some samples with higher levels of Fe loading, as shown in Fig. 4C with the 2% Fe-BTO. Further, the 1% Fe-BTO was examined with XRD after 4 h of illumination in the photocatalyst reactor, and Fig. 4D shows no sign of alteration of the material. Thus, the XRD analysis indicates that (i) the signature of the BTO phase is maintained with Fe addition, indicating that Fe is most likely introduced substitutionally within the structure and (ii) in the composition range studied here, while the added Fe is clearly manifested within the BTO at 1% doping (there is no evidence of Fe_2O_3 formation), as Fe content increases, the role of the Fe is split; partly being introduced into the BTO structure and partly participating in the formation of Fe_2O_3 . (iii) Finally, the stability of Fe-BTO shows promise for recyclability, as it is unchanged by the photocatalysis reaction on at least the scale of several hours.

3.1.5. Optical properties

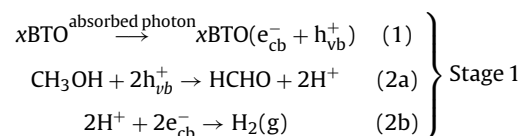
The optical responses of the BTO and Fe-BTO photocatalysts with different Fe content were measured in the diffuse reflectance mode, and the Kubelka–Munk function was used to obtain the absorbance data. Fig. 5 shows the absorbance spectra of the different photocatalysts. The BTO shows an absorbance onset at 440 nm. All Fe-BTO shows a red shift of the onset compared to the BTO. Specifically, as the Fe concentration increases, the absorbance onset is increasingly redshifted. This suggests that increased Fe presence leads to more visible light absorbance. It is noteworthy to mention that this relationship is linear in the Fe concentration region studied. Additionally, there is a small decrease in UV absorbance with increases in Fe concentration. The inset of Fig. 5 shows the photographs of the Fe-BTO with different Fe concentration. With increasing Fe content, the darkening color of the particles is evident.

3.2. Photocatalytic hydrogen generation

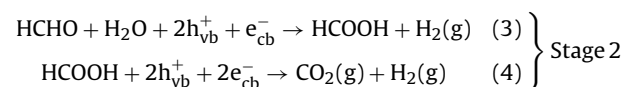
3.2.1. Effect of Fe addition

Slurry-based, as well as film-based, photocatalytic hydrogen generation is reported by several groups. Since slurry-based reactions are known to provide a higher gas yield, due to higher catalyst exposure, this approach was implemented as a preliminary test to examine the photoactivity of the catalysts. Fig. 6A shows the slurry reactor used for qualitative and quantitative testing of the photocatalysts. Qualitative analysis indicating the functionality of the catalyst under illumination, was evident from the gas collected, at thermal equilibrium, by downward displacement of a water column. Quantitative analysis indicating hydrogen formation was evident when a GC-based detection was performed. Fig. 6B shows the hydrogen produced by the catalyst in the presence and absence of Fe. The Fe-BTO demonstrates hydrogen formation, and the presence of 1% Fe doping is shown to improve the hydrogen formation by 75% compared to BTO.

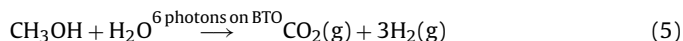
While hydrogen evolution can be performed in the absence of sacrificial agents, it has been demonstrated that without the addition of a sacrificial agent, the water acts as an inefficient electron acceptor and donor [33,34]. As a result, the oxygen radicals and protons tend to recombine to form water and very little hydrogen gas is produced [34]. The tests performed here were all in the presence of a sacrificial agent – methanol. In methanol-based systems, it is known that the methanol is consumed, leading to the formation of hydrogen. The overall steps in the hydrogen evolution process can be summarized as follows [35–37]:



Similarly,



Thus,



Photogenerated electron–hole pairs are created in the photocatalyst upon illumination (Eq. (1)). They are either trapped in the defect sites or participate in the redox processes at the photocatalyst surface. The holes oxidize the methanol forming formaldehyde (Eq. (2a)). With the holes utilized with methanol oxidation, the electrons are able to exist in the conduction band longer without recombination. The two protons evolved during methanol oxidation are reduced to hydrogen by the photogenerated electrons (Eq. (2b)) [38]. It is conjectured that at high enough formaldehyde concentration, stage 2 takes over: two more photogenerated holes interacts with one proton each from the formaldehyde and water, which the electrons then reduce to another hydrogen, the resulting hydroxyl radical, is scavenged by the formaldehyde remnant to produce formic acid (Eq. (3)) [34,35]. Finally, it is further suspected that the formic acid spontaneously dissociates to form carbon dioxide and two more protons, which allows two excited electrons to reduce the protons to a third hydrogen (Eq. (4)). In all, the photocatalyst is illuminated to generate six electron–hole pairs which split one methanol and one water molecule into a carbon dioxide and three hydrogen gas molecules (Eq. (5)), via a three-step process. It is also worth noting that this reaction, though in three steps, has been described as occurring in two stages, with the second stage producing hydrogen at a faster rate than the first [34]. We believe the inflection points seen in Fig. 6B evidence a shift

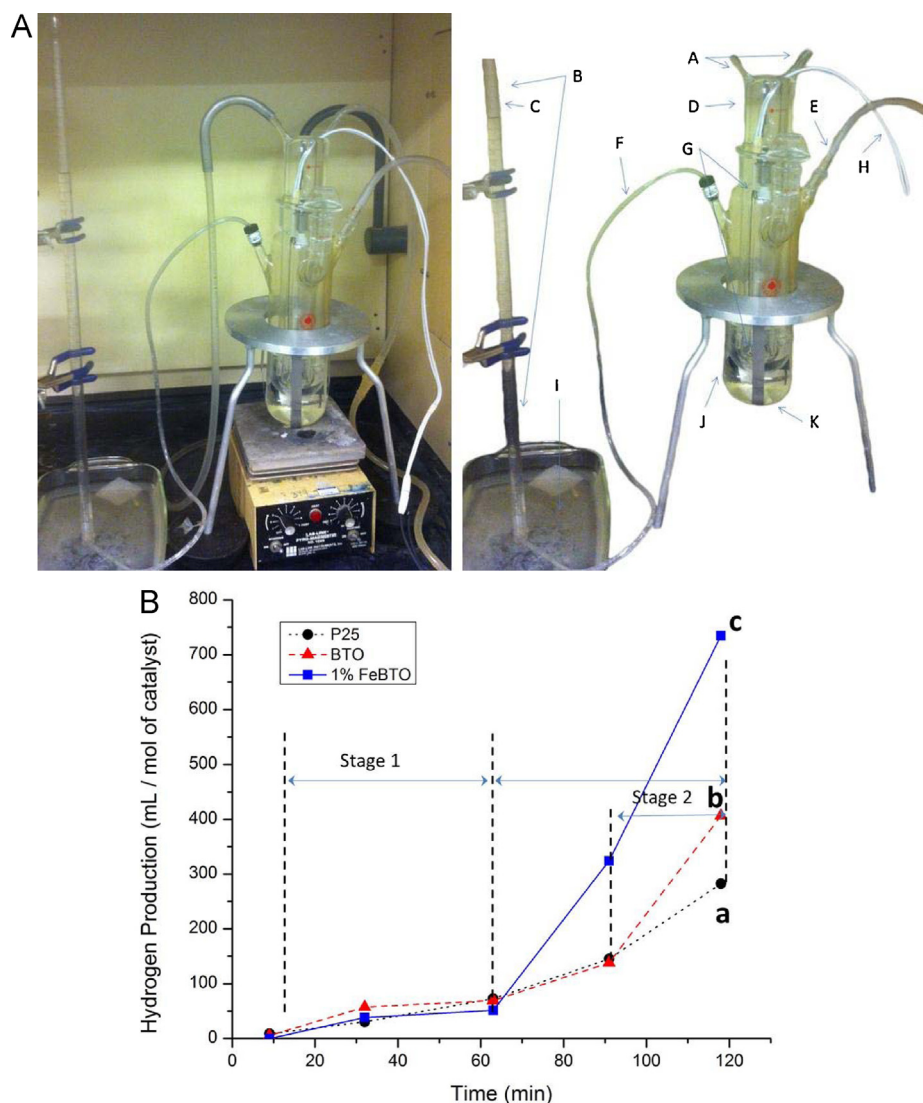


Fig. 6. (A) The photographs of the (left) complete assembly and (right) photocatalytic slurry reactor setup used for performing hydrogen generation experiments are shown. It includes: (A) cooling water lines, (B) inverted buret as water column for downward displacement gas collection, (C) collected gas, (D) water-jacketed light source cylinder, (E) argon gas sparger tube, (F) exhaust gas line (to collection column), (G) central Hg-vapor light source, (H) lamp cables (to power supply), (I) water bath, (J) methanol/water/photocatalyst slurry and (K) PTFE-coated magnetic stirrer. (B) The time resolved data showing the hydrogen yield in the presence of (a) Degussa P 25 (commercial TiO_2), (b) BTO, and (c) 1% Fe-BTO. Of particular importance is the observation of increase in the hydrogen yield with BTO and Fe-BTO after a finite incubation period marked stage 1 [For further details refer Section 2.1 in the text].

from stage 1 to stage 2 of the reaction. The shift is likely influenced by a combination of the following factors: First, the dissociation energies can lead to competition between methanol (64.1 kJ mol^{-1}) and water ($237.1 \text{ kJ mol}^{-1}$), whereas, formaldehyde has a much lower dissociation energy (47.8 kJ mol^{-1}) and depends on simultaneous water dissociation, and formic acid will spontaneously dissociate ($-95.8 \text{ kJ mol}^{-1}$). Second, different adsorption rates for methanol and the other molecules may affect the reaction rates; and finally, the solubility of hydrogen ($8 \times 10^{-4} \text{ mol/Kg(H}_2\text{O)}$) at 101 KPa and 20°C) may be causing the gas to dissolve in water, and as saturation is approached, more of the produced hydrogen is passed to the collection area. A similar inflection point for the P25 sample is not seen because it should occur near 10 h [34].

3.2.2. Effect of Fe concentration

To further probe the Fe effects, experiments were also conducted with various Fe content in the BTO. While Fig. 7A shows that

Fe doping improves the hydrogen production over BTO with up to the 2% Fe doping, any increase in doping beyond 1% Fe-BTO does not show an additional increase in the hydrogen production. This result is particularly interesting considering that the absorbance continues to show further redshift, as well as lower bandgap as shown in Fig. 7B, with increases in the Fe content. The bandgap was estimated using the following expression:

$$E = h \frac{c}{\lambda} \quad (6)$$

where E = bandgap energy, h = Planck's constant, and λ = wavelength. It is quite likely that beyond 1% Fe doping, the presence of additional Fe may be causing more trap sites which act as recombination centers, thereby reducing the number of charges for surface redox reactions. These preliminary results are encouraging nevertheless since an optimal amount of 1% Fe doping in 1% Fe-BTO is noted to produce 75% more hydrogen than pure BTO. They also open up additional questions, discussed below, that can serve as the bases for this observation.

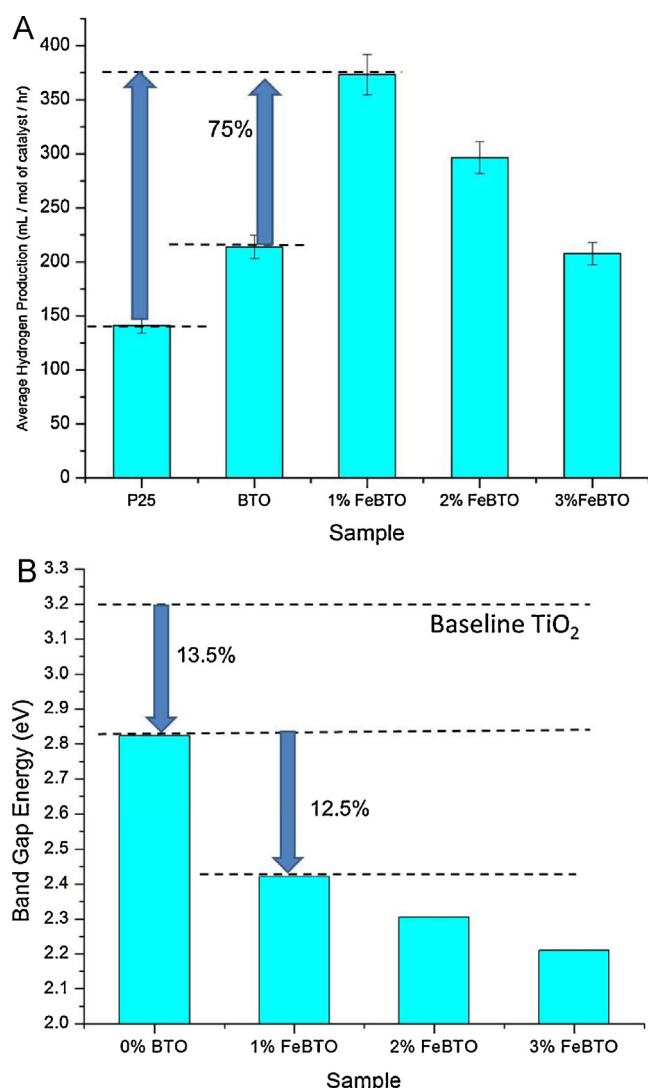


Fig. 7. (A) The bar graph showing the comparative rates of hydrogen generation using the commercial TiO_2 (Degussa P25), BTO, and BTO with various Fe content. A 75% increase in the hydrogen yield with the 1% Fe-BTO is identified as the optimal photocatalyst for hydrogen generation in this study. (B) The percent change in the bandgap of the photocatalyst with reference to the TiO_2 baseline is shown for the BTO and BTO with varying Fe-content. A 12.5% reduction in the bandgap of BTO leading to visible light absorption drives the improvement in the photocatalytic activity.

4. Discussion

4.1. Importance of Fe addition

Fe is an element that can lead to the formation of a self-compensating system when it is introduced in the BTO structure at the A and B sites. A self-compensating system involving Fe in the role of a donor as well as acceptor will help ease the synthesis and assist in making the system more stable compared to single-site Fe systems [39]. Furthermore, Fe is an abundant and inexpensive raw material with proven visible light responses. In a related study involving Fe, In, and Ga substituted for Ta in the $\text{Bi}_2\text{Ta}_2\text{O}_7$, Fe has been noted to cause the least structural distortion. A distortion tolerant structure will ensure maximum stability [39]. The scope for including other elements in the BTO structure is possible, but the photocatalytic activity is yet to be fully explored [40].

4.2. Modeling-driven predictions of additive properties

Recently, we had performed modeling studies using density functional theory (DFT) calculations and demonstrated that the introduction of Fe in the BTO lattice most enhances the visible light absorbance in comparison to other elements in the 3d group [41,42]. While, an interband state is created with all 3d elements, the one formed in the presence of Fe is closest to the valence band. Our hypothesis was that the presence of this state in BTO would translate into a better photoactive material for visible light-driven photocatalytic reactions. The composition-dependent redshift in absorbance and its subsequent effect on promoting photocatalytic hydrogen generation, as indicated in the preliminary results, validates the model.

It has been discussed that the presence of the Fe 3d band is crucial for the increased absorption of light at a lower band gap in BTO. However, with the higher concentration of Fe, the highly localized Fe 3d band would be more prominent at both valence band and conduction band edges [42], especially at the valence band maximum. This is because Fe can substitute both the Bi and Ti atomic sites in BTO. The interband state, as mentioned earlier due to Fe incorporation, would create a band due to higher concentration of Fe. Hence, two major changes would occur: (1) the electron photoexcitation will occur mainly between 3d bands of Fe (valence band) and Ti (conduction band), (2) hole effective mass will increase because of the increased Fe 3d-band presence at the valence band. This would limit both the electron and hole mobility due to the localized nature of these bands. As a result, recombination may increase. Hence, it is possible, as in Fig. 7A, higher concentration of Fe in BTO would lower the hydrogen production.

While the XRD confirms Fe introduction in the BTO structure, the exact location of the Fe and its oxidation states are unknown. The aspects such as the oxidation state and location of Fe have to be examined, using XPS and XANES to determine the level of Fe incorporation within the BTO. An in-depth study, both from experiment and theory perspective is underway, which is focused on fully comprehending the role of Fe in the oxidative processes. Currently we are examining answers to questions such as: how stable is the composite? And is there any phase segregation? Finally, the optimization which includes examining effects of light intensity and catalyst loading has to be performed to determine the maximum yield of hydrogen from the reaction.

4.3. New formulations – bandgap engineered composite oxide nanostructures (BECONs)

In a broader context, the applicability of the present work in driving the formation of new oxide composites requires mention. Single metal oxides and non-oxides have been used extensively in different photocatalytic processes. For example, Fig. 8 shows a comparison of the bandgap and band-edges of a popular oxide – n-type TiO_2 (3.2 eV). Other oxides such as InTaO_4 and a non-oxide – GaN (3.4 eV) [43] can also be used in various photocatalytic applications. Though the valence and conduction band (E_{VB} , E_{CB}) of these materials straddle a representative photocatalytic reaction, the water redox potential (1.23 eV), only UV light will drive the process. The shaded regions for E_{VB} and E_{CB} correspond to a narrower bandgap of 1.6–2.6 eV. This is the region where most visible light is available.

Unlike using additives on these large bandgap materials, using the Fe-BTO as a case study, this work demonstrates an approach to use a formulation with one structure (the pyrochlore) to achieve close to the 1.6–2.6 eV bandgap. This work lays the foundation for the development of a new family of bandgap engineered composite oxide nanomaterials, referred to as BECONs with bandgap and band edges that lie anywhere within this shaded area. Other formulations which are much better than this composition and

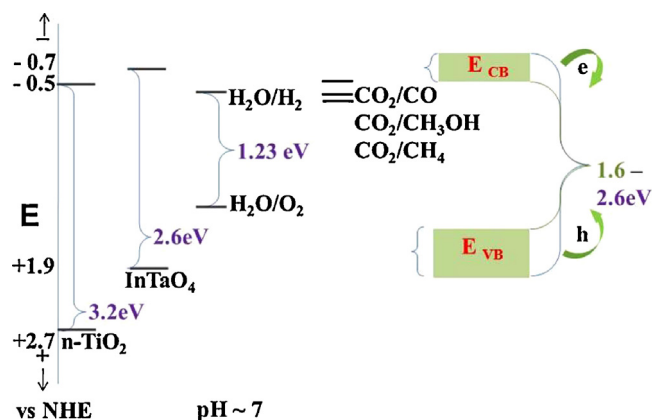


Fig. 8. Bandgap-engineered composited oxide nanostructures (BECONs) with a bandgap in the shaded region are required to perform visible light driven photocatalytic reactions.

demonstrate improved activity are very likely possible. There is an urgent need to discover BECONs with different building block elements to drive photoactivated reactions such as water splitting, photodegradation, and formation of value-added products (such as hydrocarbon fuels). It is hoped that the synthesis strategy and the preliminary proof of application demonstrated here can be used to further develop such BECONs with multi-functional properties.

5. Conclusion

A wet chemical approach to produce BTO of the pyrochlore phase with the option to introduce an earth-abundant element, Fe, without any physical changes in the features of the BTO, is presented. The surface and optical characterization of the photocatalyst has been discussed. The Fe-BTO demonstrates a size of 50 ± 15 nm and enhanced visible light absorbance compared to BTO. As the Fe doping is changed from 0% to 3% during synthesis, a steady redshift in absorbance from 440 nm to 560 nm is noted, demonstrating a decrease in the bandgap from 2.82 eV to 2.21 eV. The performance of the photocatalysts has been tested for hydrogen evolution using sacrificial methanol. Preliminary qualitative and quantitative analysis indicates that hydrogen production is higher with the inclusion of Fe and is the highest at an optimal doping of 1% Fe, with a production 75% higher than that of Fe-free BTO. The approach presented here is expected to be a universal procedure impacting the synthesis of other bandgap engineered composite oxide nanostructures (BECONs) with band edge tunability in the 1.6–2.6 eV range.

Acknowledgements

We would like to thank Dr. Mo Ahmadian for his assistance with the (HR)TEM images, for helpful insights provided by Dr. Archana Kar and Dr. Sankaran Murugesan, and preliminary experimental work by Tasha Goodrich. Partial support to this work from the Office of the Vice-President for Research at the University of Nevada, Reno for TG is also acknowledged. NSF funding (NSF-CBET 1134486) is acknowledged. EPSCoR funding fellowship and the General Undergraduate Research Award for Steven Delacruz is appreciated.

References

- [1] D.K. Ross, *Vacuum* 80 (2006) 1084–1089.
- [2] A.K. Avci, Z.I. Onsan, D.L. Trimm, *Topics in Catalysis* 22 (2003) 359–367.
- [3] A.L. Dicks, *Journal of Power Sources* 61 (1996) 113–124.
- [4] X. Chen, S. Shen, L. Guo, S.S. Mao, *Chemical Reviews* 110 (2010) 6503–6570.
- [5] B.D. Alexander, P.J. Kulesza, L. Rutkowska, R. Solarska, J. Augustynski, *Journal of Materials Chemistry* 18 (2008) 2298–2303.
- [6] J.R. Bolton, *Solar Energy* 57 (1996) 37–50.
- [7] V.M. Aroutiounian, V.M. Arakelyan, G.E. Shahnazaryan, *Solar Energy* 78 (2005) 581–592.
- [8] M. Kitano, K. Tsujimaru, M. Anpo, *Topics in Catalysis* 49 (2008) 4–17.
- [9] K. Rajeshwar, *Journal of Applied Electrochemistry* 37 (2007) 765–787.
- [10] M. Ni, M.K.H. Leung, D.Y.C. Leung, K. Sumathy, *Renewable & Sustainable Energy Reviews* 11 (2007) 401–425.
- [11] Y.A. Shaban, S.U.M. Khan, *International Journal of Hydrogen Energy* 33 (2008) 1118–1126.
- [12] C. Li, J. Yuan, B. Han, L. Jiang, W.F. Shangguan, *International Journal of Hydrogen Energy* 35 (2010) 7073–7079.
- [13] H. Park, W. Choi, M.R. Hoffmann, *Journal of Materials Chemistry* 18 (2008) 2379–2385.
- [14] K. Kalyanasundaram, M. Gratzel, *Proceedings of the Indian Academy of Sciences: Chemical Sciences* 109 (1997) 447–469.
- [15] P. Cheng, M.Y. Gu, Y.P. Jin, *Progress in Chemistry* 17 (2005) 8–14.
- [16] P.D. Cozzoli, E. Fanizza, R. Comparelli, M.L. Curri, A. Agostiano, D. Laub, *Journal of Physical Chemistry B* 108 (2004) 9623–9630.
- [17] K. Rajeshwar, N.R. de Tacconi, C.R. Chenthamarakshan, *Chemistry of Materials* 13 (2001) 2765–2782.
- [18] I. Robel, V. Subramanian, M.K. Kuno, P.V. Kamat, *Journal of the American Chemical Society* 128 (2006) 2385–2393.
- [19] A.J. Frank, N. Kopidakis, J. van de Lagemaat, *Coordination Chemistry Reviews* 248 (2004) 1165–1179.
- [20] W.Y. Choi, A. Termin, M.R. Hoffmann, *Angewandte Chemie International Edition* 33 (1994) 1091–1092.
- [21] M.A. Subramanian, G. Aravamudan, G.V.S. Rao, *Progress in Solid State Chemistry* 15 (1983) 55–143.
- [22] T. Kako, Z. Zou, J. Ye, *Research on Chemical Intermediates* 31 (2005) 359–364.
- [23] L.L. Garza-Tovar, L.M. Torres-Martinez, D.B. Rodriguez, R. Gomez, G. del Angel, *Journal of Molecular Catalysis A: Chemical* 247 (2006) 283–290.
- [24] Z.G. Zou, J.H. Ye, H. Arakawa, *Topics in Catalysis* 22 (2003) 107–110.
- [25] A. Kudo, H. Kato, S. Nakagawa, *Journal of Physical Chemistry B* 104 (2000) 571–575.
- [26] S. Murugesan, V. Subramanian, *Chemical Communications* 45 (34) (2009) 5109–5111.
- [27] S.J. Henderson, O. Shebanova, A.L. Hector, P.F. McMillan, M.T. Weller, *Chemistry of Materials* 19 (2007) 1712–1722.
- [28] H.J. Zhou, T.J. Park, S.S. Wong, *Journal of Materials Research* 21 (2006) 2941–2947.
- [29] Zhenfeng, Z. Bian, Y. Huo, Y. Zhang, J. Zhu, Y. Lu, H. Li, *Applied Catalysis B: Environmental* 91 (2009) 247–253.
- [30] W.F. Yao, H. Wang, X.H. Xu, J.T. Zhou, X.N. Yang, Y. Zhang, S.X. Shang, *Applied Catalysis A: General* 259 (2004) 29–33.
- [31] W.F. Yao, H. Wang, X.H. Xu, X.N. Yanga, Y. Zhanga, S.X. Shang, M. Wanga, *Applied Catalysis A: General* 251 (2003) 235–239.
- [32] H. Zhou, T.J. Park, *Journal of Materials Research* 21 (2006) 2941–2947.
- [33] H.J. Choi, M. Kang, *International Journal of Hydrogen Energy* 32 (2007) 3841–3848.
- [34] X. Yang, C. Salzmann, H. Shi, L. Malcolm, H. Green, T. Xiao, *Journal of Physical Chemistry C* 112 (2008) 10784–10789.
- [35] J. Chen, D.F. Ollis, W.H. Rulkens, H. Bruning, *Water Research* 33 (1999) 669–676.
- [36] J. Chen, D.F. Ollis, W.H. Rulkens, H. Bruning, *Water Research* 33 (1999) 1173–1180.
- [37] D.F. Ollis, *Topics in Catalysis* 35 (2005) 217–223.
- [38] R. Gao, J. Stark, D.W. Bahnemann, J. Rabani, *Journal of Photochemistry and Photobiology A: Chemistry* 148 (2002) 387–391.
- [39] J.H. Wang, Z.G. Zou, J.H. Ye, *Journal of Physics and Chemistry of Solids* 66 (2005) 349–355.
- [40] R. Abe, M. Higashi, K. Sayama, Y. Abe, H. Sugihara, *Journal of Physical Chemistry B* 110 (2006) 2219–2226.
- [41] S. Murugesan, M.N. Huda, Y. Yan, M.M. Al-Jassim, V. Subramanian, *Journal of Physical Chemistry C* 114 (2010) 10598–10605.
- [42] M.N. Huda, A. Walsh, Y.F. Yan, S.H. Wei, M.M. Al-Jassim, *Journal of Applied Physics* 107 (2010) 123712.
- [43] J.D. Beach, R.T. Collins, J.A. Turner, *Journal of the Electrochemical Society* 150 (2003) A899–A904.